Deep-learning climate emulator ACE2 reveals a global decrease in tropical cyclone frequency in the 15th Century under an El Niño-like sea surface temperature pattern

Mu-Ting Chien[1], Wenchang Yang[2], Eric D. Maloney[3], Gabe Vecchi[2], & Elizabeth A. Barnes[1,2,3]

[1] Faculty of Computing and Data Sciences, Boston University, USA
[2] Department of Geosciences, Princeton University, USA
[3] Department of Atmospheric Science, Colorado State University, USA
[4] Department of Earth and Environment, Boston University, USA

Contact: Mu-Ting Chien (mchien@bu.edu)

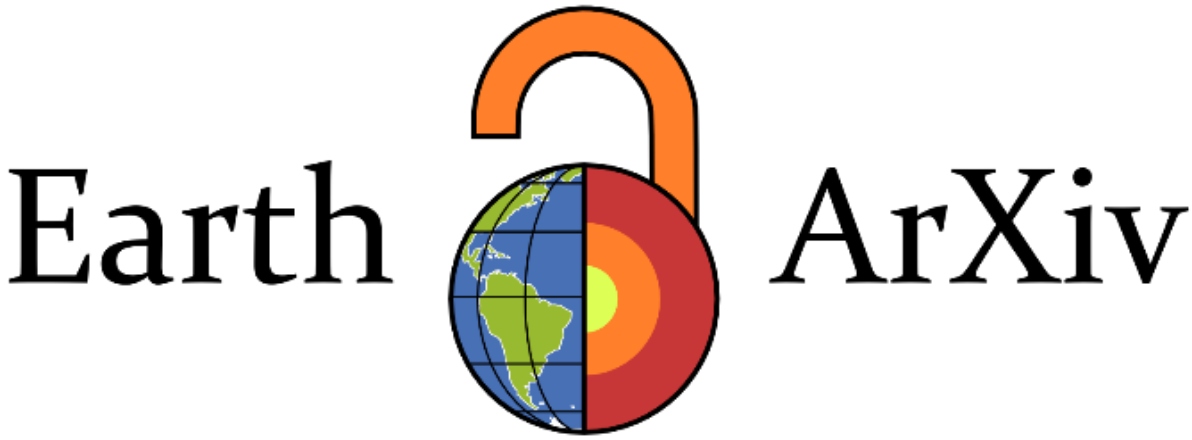

Submitted to Science Advances in Mar 3, 2026

Science Advances Manuscript Template
AAAS

Front Matter

Title

Deep-learning climate emulator ACE2 reveals a global decrease in tropical cyclone frequency in the 15th Century under an El Niño-like sea surface temperature pattern

Authors

Mu-Ting Chien,[1]*, Wenchang Yang[2], Eric D. Maloney[3], Gabriel A Vecchi[2], & Elizabeth A. Barnes[1,3,4]

Affiliations

[1] Faculty of Computing and Data Sciences, Boston University, USA.
[2] Department of Geosciences, Princeton University, USA.
[3] Department of Atmospheric Science, Colorado State University, USA.
[4] Department of Earth and Environment, Boston University, USA.

Abstract

The relatively short modern observational record limits our understanding of the relationship between global tropical cyclone (TC) frequency and sea surface temperature (SST), resulting in uncertain future TC projections. Using novel deep-learning-based past-millennium simulations with the Ai2 Climate Emulator version 2 (ACE2), we provide insight into the connections between SSTs and TCs. ACE2 simulations reveal that the Atlantic and global tropical cyclone numbers decreased in the 15th Century under an El Niño-like SST pattern, consistent with the high-resolution dynamical climate model HiRAM, and Atlantic sediment proxies. Global TC frequency decreased mainly due to stronger vertical wind shear and the drier midtroposphere as the Hadley circulation strengthened. Conversely, global TC frequency would increase under a La Niña-like SST pattern, as shown in idealized SST experiments with ACE2. This study demonstrates an exciting opportunity to examine TC-climate interactions using deep-learning-based paleoclimate simulations and highlights the need to constrain future projections of SST patterns to accurately estimate TC frequency.

Teaser

Global and North Atlantic tropical cyclones decline under equatorial warming, revealed by past-millennium deep-learning simulations and sediments.

MAIN TEXT

Introduction

Since all impacts of tropical cyclones (TCs) require the existence of a TC, accurate predictions of annual tropical cyclone (TC) frequency lead to better societal planning for damage mitigation. However, predicting TC frequency remains challenging because our understanding of its relationship with large-scale climate is limited, owing to the complexity of multi-scale interactions and the short modern instrumental record (1). To date, no significant trend in global TC frequency has been observed in the short instrumental record (~80 years), even with the emergence of a climate change signal in surface temperatures (1, 2). Future projections of tropical cyclone numbers under climate change also remain uncertain (3), with many global climate models suggesting a global decrease in TC frequency, and other models and statistical downscaling studies predicting a global increase in TC frequency under warming scenarios of the 21st Century (1-6). These conflicting results indicate a lack of consensus on how large-scale climate (i.e., sea surface temperature (SST) patterns) would change under greenhouse gas-induced warming (7) and how they control the global tropical cyclone frequency (7-11).

Examining tropical cyclone frequency over the past millennium, long before the modern instrumental era, is a promising way to disentangle the relationship between long-term climate states (or SST patterns) and TC frequency (12-15). When examining the past, scientists use proxy data from corals, tree rings, and ocean sediments to infer past SSTs (16) and even approximate the number of tropical cyclones in some regions (14, 15). However, these paleo proxy data are sparse in space and time, and thus, global simulations are often necessary to obtain output that is spatially consistent and temporally continuous. Numerical simulations of TCs are traditionally performed by high-resolution global climate models that have a good representation of TC numbers (3), but are extremely expensive to run. The latest evidence from sediment-based TC proxies suggests that one of the largest decreases in Atlantic TC numbers over the past millennium occurred between 1351 AD and 1550 AD, as the climate transitioned to the Little Ice Age (15). However, (15) did not run high-resolution global climate models that explicitly resolve TCs, making it difficult to comprehensively discuss what environmental factors may have led to this possible TC change.

In recent years, deep-learning climate emulators (AI emulators) have emerged and offer more simulations at lower computational costs, potentially serving as an alternative tool for long-term climate simulations (17-21). These AI emulators are trained on reanalysis or dynamical global climate models and demonstrate good representation of climate variability (17-20), and even extreme weather events (22, 23, 24). AI emulators have been shown to exhibit a realistic representation of past heatwaves and cold events up to the beginning of the 20th century, decades outside of their training period (25). While tropical cyclone (TC) variability and its relationship with environmental conditions in the current climate are found to be well simulated in a deep-learning emulator, the Ai2 Climate Emulator Version 2 (ACE2) (22, 23), the extent to which AI emulators can be used to simulate climates outside of their historical training period (e.g., the past millennium) is currently at the forefront of their uptake. If the AI emulators can simulate the past millennium TCs well, they will provide a unique opportunity to examine TC-climate interactions through various experiments at high computational efficiency — a novelty of this study.

Driving questions for this research are as follows: First, how well can a deep-learning climate emulator, ACE2, simulate global TC frequency changes during the transition to the Little Ice Age, specifically from 1351 to 1550 AD? Second, what role did SSTs play in

modifying global TC frequency from 1351 to 1550 AD? Examining preindustrial climate allows us to focus on the natural variability of TC frequency and SSTs. By combining the efficiency of a deep-learning climate emulator with paleoclimate records, we aim to build a fundamental understanding of SST patterns and global TC frequency.

We perform the first sets of TC-resolving global simulations from 1351 to 1550 AD using (i) a deep-learning climate emulator ACE2 and (ii) a high-resolution dynamical model HiRAM forced with the SST boundary conditions. The simulations are compared with sediment proxy data of Atlantic tropical cyclones as our baseline for validation. We also systematically examine the effects of SSTs on global TC frequency by running various idealized SST pattern experiments in ACE2, fully leveraging the fast computation of ACE2. Our paleo TC diagnostic using the seed-probability framework (26-28) has implications for future changes in TC frequency.

Results

Atlantic and global TC decreases in the 15th century

We force ACE2 and HiRAM with SSTs and sea ice from 1351 to 1550 AD using last-millennium reconstruction datasets (LMR 2.1, 16, 29) and track TCs across the simulations using 6-hourly data (see Materials and Methods). Global TC frequency across all ACE2 ensemble members depicts a clear decrease in the 15th century (from 1401 to 1500 AD), in agreement with the single HiRAM simulation (Fig. 1A). The global TC frequency decreases by 13.1% from the highest activity during 1401-1420 AD (hereafter termed the High period) to the lowest activity during 1461-1480 AD (hereafter termed the Low period) in the ACE2 ensemble mean. The ensemble mean annual TC counts drop by 13.2% (from 37.8/year to 32.8/year). The simulated decrease in TC frequency occurs across all ACE2 members in most basins except the Western Pacific (green shading in Fig. 1B). Focusing on the Atlantic Ocean, the Atlantic 40-year lowpass TC number also decreases in all members of ACE2 and a single member of HiRAM in the 15th Century (Fig. 2A).

The simulated Atlantic TC frequency change in the 15th century is validated by the sediment-overwashed proxy of Atlantic TC number (see Materials and Methods), also showing more TCs in the early 15th century and fewer TCs in the late 15th century (Fig. 2B). Although the exact timing of the peaks and troughs of TC activity slightly differ across ACE2 members and sediment proxy (due to internal atmospheric variability), the overall decrease in Atlantic TC activity in the 15th century is consistent across all data sources (Fig. 2, Fig. S1). The sediment-based proxy data are currently the best estimate of Atlantic TC activity over the past millennium (15). This estimation generally agrees with modern observations of TCs, although some discrepancies remain in the mid-19th century and late 20th Century likely due to the limited number of sites. The sediment-based estimation of Atlantic TC activity over the past millennium depicts one of the largest drops in the 15th century (i.e., roughly the beginning of the Little Ice Age) (15), motivating our study to focus on this period.

Despite the constraints of each dataset: the dynamical HiRAM model (e.g., the use of cumulus parameterization), the AI emulator (e.g., trained on the current climate reanalysis), and the sediment-based TC estimate (e.g., limited site numbers), three lines of evidence show the same signal that Atlantic TC frequency decreased in the 15th century.

The reconstructed temperature and sea ice data used to force the ACE2 and HiRAM simulations are based on estimates from coral reefs, tree rings, and sediment and ice core measurements, and are thus independent of the sediment-overwashed estimate of TC numbers. Validation of the Atlantic TC change across ACE2, HiRAM, and the sediment proxy indicates that both simulations are likely comparable to observations, supporting the realism of the global TC decrease in the 15th century (Fig. 1A). These results further support that the AI climate emulator may learned the relationship between TC frequency and SST patterns from the training data in the current climate.

But why did TC activity decrease in most basins from the High to the Low period in the 15th century (Fig. 1B)? The consistent decrease in global TC frequency in ACE2 and HiRAM is most likely due to their shared SST forcing. The global mean SST decreased by 0.5 K from the High (1401-1420 AD) to the Low (1461-1480 AD) period (Fig. 1C), with all tropical oceans but the warm tongue exhibiting cooling from the High to the Low period (Fig. 1D). Two major volcanic eruptions, which produced over 10 Tg stratospheric sulphate injection, occurred in 1452-1453 AD and 1459-1460 AD (green lines in Fig. 1C) (30). The volcanic eruptions likely contributed to the cooling of the global mean temperature during the Low period, as they released sulfate aerosols into the stratosphere, which blocked incoming solar radiation to the surface (30). One possible hypothesis for the global decrease in TC frequency is attributed to the global mean SST cooling. The theoretical basis for this argument is that TCs occur only when SSTs are sufficiently warm to provide an abundant sensible and latent heat source (31), which aligns with some dynamical models and the statistical downscaling approach that predicts an increase in TC activity with warming (3-5).

On the other hand, SST patterns (rather than the global mean SST) have also been shown to affect regional TC frequency (7-11). Expanding on this idea, here, we focus on the changes in SST patterns between the High and Low periods. SST decreased in most tropical oceans, except that warming occurs in the equatorial cold tongue region in the Pacific, resembling an El Niño-like anomaly pattern (Fig. 1D).

The deviation of global mean SST over the entire period (1401-1500 AD) from the current climate (1950-1980) is less than 0.2 K; this small deviation is within the interannual variability of SST during the training period of ACE2, further supporting the possible use of ACE2 to investigate this paleo period.

A natural question arises: Was the decrease in global TC frequency resulted from global mean SST cooling or from the specific SST pattern? This motivates us to perform idealized experiments with different SST patterns by leveraging the computational speed of ACE2.

Global TC decreases under an El Niño-like SST trend

We perform several idealized time-slice experiments with different SST patterns in ACE2 to decompose the effects of the anomalous SST mean and pattern on global TC frequency changes (see Materials and Methods for details). The control run (CTL) represents the High period, prescribed with the climatological mean SST between 1401 and 1420 AD. The SST of CTL shows a similar Indo-Pacific and Atlantic warm pool as in the current climate (Fig. S2B). Experiment 1 (EXP1) represents the Low period, as prescribed by the mean SST between 1461 and 1480 AD. The SST anomaly in EXP1 relative to the CTL resembles an El Niño-like pattern (Fig. 1D and Fig. 3A), except that stronger cooling occurs on the west coast of Mexico over the Eastern Pacific. We also run three additional

experiments with SST anomalies modified from EXP1 to test the importance of equatorial cold-tongue warming/cooling, while keeping the global mean SST the same as in EXP1. Thus, comparing the response of global TC frequency to different SST patterns directly tells us the effect of SST patterns under the same global mean cooling. We run the CTL for 80 years (i.e., 80 ensemble members) and the remaining four experiments (EXP1-EXP4) for 40 years, with each year representing a different ensemble member (i.e., 40 ensemble members). The initialization is described in the Materials and Methods. Performing these experiments is only possible thanks to the high computational speed of AI emulators.

Under El Niño-like SST change (EXP1), almost 75% of the 40 members predict a decrease in TC number compared to CTL, yielding a p-value of 0.0032 from binomial testing (Fig. 3E, see Materials and Methods for details of statistical test). In other words, the global decrease in TC frequency (about 3 TCs, as shown in Fig. 3F, black bar) is significant at the 99.9% confidence level. TC frequency decreases in most basins in EXP1, except in the Western Pacific, where TC frequency slightly increases (Fig. 3F). Overall, this leads to a 7.5% decrease in global TC frequency.

If warming occurs only over the equatorial cold tongue with uniform cooling elsewhere (EXP2, Only-cold-tongue-warming, Fig. 3B), the global TC frequency is still more likely to decrease, although the significance level is lower than in EXP1 (Fig. 3E). The decrease in global TC frequency in the Only-cold-tongue-warming (-3.5%) comes from the decrease in TCs in several basins, including the Northeastern Pacific (NEP), the North Atlantic (NATL), and the Southern Indian Ocean (SI) (Fig. 3G). The fact that TC frequency is still more likely to decrease at the 87% confidence level suggests that equatorial cold-tongue warming may play a significant role in the global decrease in TC frequency.

The response of global TC frequency in the absence of cold-tongue warming is much less clear (EXP3, No-cold-tongue-warming, Fig. 3C) (Fig. 3E). Although the global mean TC frequency still decreases (-2.7%), the decrease is less so than in Experiment 1, due to a compensating effect of increasing TCs in NWPAC and decreasing TCs in NEP and NIO (Fig. 3H).

Moreover, global TC frequency increases under cold-tongue cooling (EXP4, La Niña-like, Fig. 3D) at a significance level of 99.5% or higher (Fig. 3E). Global TC increases by 2.9% in this experiment due to an increased TC activity in most basins except NEPAC (Fig. 3I).

In summary, compared to the mean and median global TC number in CTL, the El Niño-like and Only-cold-tongue-warming experiments show lower TC activity, the No-cold-tongue-warming experiment shows similar TC activity, and the La Niña-like experiment shows higher TC activity (Fig. S3). These experiments suggest that if the equatorial cold-tongue does not exhibit a large anomaly, the resulting TC frequency change is less robust, as shown by the biggest interquartile range in the No-cold-tongue-warming experiment among all experiments (Fig. S3). From this we conclude that equatorial warming/cooling strongly influences whether global TC frequency decreases or increases.

These idealized experiments establish a strong link between the global TC frequency change and the cold-tongue SST variability, rather than the global mean SST change. While the cold-tongue SST warming is associated with global TC decrease, cold-tongue SST cooling is associated with global TC increase.

Why does global TC frequency decrease under an El Niño-like SST change?
We adopt the seed-probability framework (26-28) to examine why the global TC frequency decreases under the El Niño-like SST pattern from CTL to Experiment 1. The framework assumes tropical cyclogenesis as a two-step process: first, forming the precursor disturbance (i.e., seeds), and second, these seeds intensifying into TCs. This framework approximates the number of TCs as the number of seeds multiplied by the probability of intensifying to a TC:

$$N_{TC} = N_{Seed} * \text{Probability}. \quad [1]$$

Probability is calculated from three monthly mean environmental conditions (26, see Materials and Methods for more details), including (i) the potential intensity (PI), the theoretical likelihood of TCs to intensify based on the heat engine assumption, with the efficiency of the heat engine proportional to the temperature difference between the surface and the upper troposphere, (ii) the vertical wind shear (shear), which is the magnitude of the horizontal vector wind difference between 850 and 200 hPa, and (iii) the moist entropy deficit (moist), which is the ratio between the mid-troposphere moisture deficit and the boundary layer moisture deficit; a larger moist entropy deficit represents a drier mid-troposphere under the same boundary layer moisture. The probability of a seed intensifying into a TC is largest in the Northwestern Pacific and Southern Pacific to the west of the dateline (180°E) in CTL (Fig. S4A), mainly due to lower saturation moisture deficit (moister mid-troposphere) (Fig. S4B), larger potential intensity (Fig. S4C), and smaller vertical windshear (Fig. S4D).

We also explicitly track seeds in CTL and EXP1 (see Materials and Methods) from ACE2. The number of seeds is generally 2.6 times that of TCs because not all seeds become TCs (Fig. S5). Despite different seasonal cycles of seeds and probability (Fig. S6, solid vs. dashed lines), the seasonal cycle of seeds multiplied by probability (Fig. 4A-F, dotted line) can capture the seasonal cycle of simulated TCs (Fig. 4A-F, solid line). For example, in the North Atlantic, the change in seeds shows a more drastic onset after June, while the change in probability is more gradual (Fig. S6); however, considering seeds and probability together better captures the seasonality of observed TCs (Fig. 4C, 27). Using seeds and probability together can capture the seasonal cycle of TCs across all basins, with a linear regression coefficient of =0.92 (Fig. 4G). Thus, TC genesis in ACE2 is likely physical (22, 23), and we can use the seed-probability framework to analyze the decrease in global TC frequency from CTL to Experiment 1 (Fig. 5G).

The global decrease in TC frequency from CTL to EXP1 is mostly driven by a decrease in transition probability (relative contribution 80.6%), while the decrease in seeds contributes only slightly (relative contribution 19.2%) (Fig. 5O). The relative contribution is quantified by fixing either probability or seeds as in CTL, and comparing with the actual TC change. Global seed number shows little change from CTL to EXP1, due to compensating effects of increased seeds in SWPAC and NWPAC and decreased seeds in other basins (Fig. 5B, 5H). Contrastingly, the probability decreases in all off-equatorial basins (polar to 10N/S) where TCs typically form (Fig. 5C, I). Probability change is the dominant driver of the global TC decrease, regardless of the different seed-tracking criteria we used (Fig. S7).

Among all factors that affect probability, the saturation moisture deficit and wind shear together account for 68.6%, and the contribution due to potential intensity is 13.1% (Fig. 5O). The probability for each factor is quantified using monthly data for that factor in

EXP1, while keeping the other factors fixed as in CTL. The probability change due to vertical wind shear qualitatively resembles the overall probability change, showing an overall decrease in off-equatorial regions, with some increase in some equatorial regions and the Eastern Pacific (Fig. 5D). Furthermore, the probability change due to saturation moisture deficit shows an overall global decrease in all basins except in the equatorial Pacific (Fig. 5E, K), resembling the probability change due to all factors despite a lower magnitude. On the other hand, the change in probability due to potential intensity is small compared to the total probability, suggesting that potential intensity is not the dominant reason for the probability drop (Fig. 5F). The probability change across the ACE2 ensemble due to each factor is consistent with that of the single ensemble member of HiRAM (Fig. S8), showing increasing shear and mid-tropospheric drying in the 15th Century.

In summary, global TC frequency decreases under El Niño-like SST because equatorial warming (Fig. 6A) favors stronger equatorial convection (Fig. 6B), which strengthens the Hadley circulation and, in turn, is associated with stronger subsidence drying and larger wind shear in the off-equatorial regions (Fig. 6C, 6E). Drier mid-troposphere and larger wind shear hinder TC genesis. The change in the meridional overturning circulation and its effect on TC genesis is consistent across SST experiments. As the meridional SST gradient increases across experiments (from La Niña-like to El Niño-like experiment), annual TC number decreases consecutively with the decrease in seed-to-TC probability (Fig. 7A), mainly driven by the increasing vertical wind shear and larger saturation moisture deficit (Fig. 7B, S9, S10). Overall, the change in the meridional SST gradient largely determines whether global TC frequency increases or decreases by modifying the strength of the meridional general circulation. Our results show a strong link between global TC frequency and SST patterns, particularly the meridional SST gradient, providing insights into future TC projections.

On a separate note, the regional TC change in each basin under an El Niño-like pattern is more complicated than the global change, as it is a tug-of-war between regional changes in probability and seed (Fig. 5G, H, I). For example, in the South Pacific (SPAC), the strong probability decreases under an El Niño-like pattern outweigh the increase in seeds, leading to a decrease in TC frequency. In the Northwestern Pacific (NWPAC), however, the increase in seeds outweighs the decrease in probability, leading to an increase in TC frequency. The El Niño-like pattern induces stronger equatorial convection in the central Pacific, which also increases the seed propensity index (likelihood of seed genesis based on large-scale upward motion; see 26 and Materials and Methods) right off the equator over the Pacific (Fig. 6D), where planetary vorticity is nonzero. This leads to increased seed counts in SPAC and NWPAC, thereby affecting regional TCs (Fig. 6F). Globally, however, a small change in seed number contributes only slightly to changes in global TC frequency (Fig. 5O).

Discussion

We demonstrate a framework to investigate tropical cyclone (TC) frequency in paleoclimate, specifically during the transition to the Little Ice Age (1401-1500 AD), using a deep-learning global climate emulator (ACE2), and compare it with dynamical model simulations (HiRAM), and sediment proxy data. We show the exciting possibility of using ACE2 to perform various idealized sea surface temperature pattern experiments,

fully leveraging its fast computation to diagnose the drivers of SST-driven global TC variability. Our results suggest that SST patterns, given the same global-mean cooling, largely determine whether global TC frequency increases or decreases – underscoring the need to understand the mechanisms controlling patterns of SST change in efforts to understand the drivers of past TC activity and predict future TC activity. Under an El Niño-like SST pattern, the meridional SST gradient is larger, favoring a stronger meridional overturning circulation with larger wind shear and a drier mid-troposphere, producing an environment less favorable for TC genesis (Fig. 8). La Niña-like SST patterns are more favorable for TC genesis as the meridional overturning circulation weakens. Under the seed-probability framework, the overall change in global TC frequency is dominated by changes in seed-to-TC transition probability due to wind shear and mid-tropospheric humidity, whereas regional TC changes are highly dependent on changes in both seeds (i.e., precursor disturbances) and probability.

Our results have implications for future projections of tropical cyclone frequency, as many global climate models predict an El Niño-like warming pattern, whereas the observational record over the current decades shows a La Niña-like warming pattern (7). We underscore the need to better constrain SST projections to obtain more accurate estimates of future tropical cyclone activity. Our results add to the growing literature emphasizing that the pattern of SST trend has a large influence on TC frequency (7-11), with a unique perspective of examining global TC frequency under the past millennium climate. A few potential future research directions include expanding the time span of this analysis to the entire last millennium, to find if an El Niño-like or La Niña-like trend occurs during other time periods, and how global TC frequency changes in response. To further test our finding (i.e., the sensitivity of global TC frequency to equatorial warming) across mean climate states, future studies can conduct more idealized SST experiments based on the present-day mean SST with small regional patches of warming all over the globe (e.g., the Green's function approach, 37), and systematically examine the sensitivity of global TC frequency to regional warming (38). Meanwhile, the TC-SST investigation would also benefit from the development of next-generation AI climate emulators with more vertical levels and a more accurate representation of upper-tropospheric temperatures (see Materials and Methods).

While future projections of TCs are highly uncertain, we demonstrate that examining TC variability over the last millennium can provide insights into TC-climate interactions, providing a complementary lens to exploring the modern instrumental era. The last millennium provides long enough data to gain insights that we cannot obtain from recent trends after the instrumental era, and the preindustrial climate provides a natural laboratory for examining changes in TC frequency. For this approach to work, TC-resolving simulations are necessary, and for this, we highlight the success of a deep-learning emulator (ACE2). However, to comprehensively investigate past-millennium TC-climate interactions, we stress the need to develop more proxy data on TC in other major TC basins, such as the Western Pacific (13). More proxy data will allow us to fully leverage past-millennium simulations from dynamical models and AI emulators with high confidence.

Materials and Methods

Ai2 Climate Emulator (ACE2)

ACE2 is the second version of the Ai2 Climate Emulator (19). It is trained on the

ERA5 reanalysis dataset (34) from 1940 to 2000, and 2010-2020. The architecture is based on spherical Fourier Neural Operators (35), with an autoregressive prediction of temperature, horizontal wind, humidity, surface pressure, and precipitation. The prediction is at 6-hourly temporal resolution with 8 vertical levels on a sigma-pressure hybrid coordinate. Forcing variables are prescribed, including SST, sea ice fraction, CO2 concentration, and shortwave radiation. A unique advantage of this emulator is that it conserves global air mass and moisture, which makes long-term integration possible. ACE2 is a good candidate for climate modeling because it can be run stably for more than 1000 years with low computational resources.

High-resolution atmospheric model (HiRAM)
In addition to ACE2, we also use the Princeton Geophysical Fluid Dynamics Laboratory dynamical high-resolution atmospheric model (HiRAM), with 50-km horizontal resolution, and 37 vertical levels (36). This model has shown good skill in representing global tropical cyclone activity (37).

Sediment proxy data of Atlantic TC
In the Atlantic Ocean, studies have provided sediment proxy data from 12 sites along the east coast of the US and the islands of the Caribbean Sea to construct the basin-wide Atlantic TC activity (15). The sediment-based TC proxy data is our best estimate of the basin-wide TC frequency in the North Atlantic over the past millennium. The sediment data examines the number of event layers to approximate the number of tropical cyclones. That is, when intense storms pass over the island, the intense rainfall and wind make coarse-grained particles in the sediment more likely to occur than during normal times without storms. While the sediment data are collected at different locations, a recent study (15) used those data to construct basin-wide Atlantic TC activity. They combined data from each site, removed duplicate TC cases, normalized by the modern observations at each site, and smoothed with a 40-year low-pass filter to match the coarsest resolved contributing record from an individual site. Although the sediment proxy is our best estimate of Atlantic TC, it should be noted that the data are based on a limited number of sites, including a complete lack of proxy data in the Southern Caribbean, Western Gulf Coast, and Southeast US coast.

Paleo experiment using ACE2
We run 3 members of the ACE2 simulation with prescribed boundary conditions from 1351 to 1550 AD. The boundary conditions come from solar forcing, the last-millennium reconstructed sea surface temperatures (SSTs) and sea ice, and CO2 concentrations held at the preindustrial level of 280 ppm. Sea surface temperature is reconstructed from data assimilation of proxy data, including temperature from coral reefs, ocean sediment, and ice cores (LMR 2.1, 16). The northern hemispheric sea ice uses the reconstruction from (29), while the Southern hemispheric sea ice is set to the average between 1940 and 1970, since no reconstruction data are available to our knowledge. Because the reconstructed SST and sea ice data are only provided annually, we obtain the 6-hourly forcing by adding the average annual cycle from 1940 to 1970 in the ERA5 reanalysis at 6-hourly resolution to the annual reconstructed SST and sea ice. Solar forcing is prescribed to be the same as present, representing the seasonal cycle based solely on orbital parameters. Because no observed atmospheric initial condition of 1351 AD exists, we obtain the initial condition by running the ACE2 model for 1 year with the initial condition from the 1940 ERA5 reanalysis and 1350 AD boundary conditions. This initial condition is

used for the first member. To obtain the initial condition of the second member, we take the initial condition of member 1 and run ACE2 with the boundary condition of 1350 AD for another year, and get the final output. Similarly, we take the initial condition of member 2 and run ACE2 with a boundary condition of 1350 ad for one more year, and get the final output as the initial condition of member 3. After getting the three initial conditions, we run the ACE2 with forcings from 1351 to 1550 AD.

Paleo experiment using HiRAM
We take a similar approach as those above in ACE2, except that (i) we only run one member of HiRAM, due to the high computational expense, (ii) we use the sea ice monthly climatology over 1871-1890 from HadISST, instead of using the sea ice data from reconstruction, and that (iii) SST is from LMR2.1 with bias correction following (38).

Idealized sea surface temperature experiments with ACE2
In addition to the temporal evolution experiment as mentioned before, we have 5 sets of time-slice experiments using different SST patterns as boundary conditions, named the control run (CTL), and experiments 1-4. While the control run is run for 80 years (i.e., 80 ensemble members), the remaining four experiments are run for 40 years, with each year representing a different ensemble member. The first member of CTL (EXP1-EXP4) is initialized by the initial condition of 1401 (1461) AD. The initial condition for 1401 (1461) AD is obtained by running the ACE2 model for 1 year with SST boundary conditions of 1400 (1460) AD. The initial conditions for the remaining members are obtained from the last day of the 1-year simulation of the previous member. That is, the second (third) member of the simulation is initialized by the last day of the 1-year simulation of the first (second) member, and so on. The SST pattern of the control run is based on the climatology of the year 1401-1420, when global TC activity maximizes during the 1351-1550 AD period. The SST of the first experiment (EXP1) is obtained from the climatology of the year 1461-1480 AD, when the global TC activity is minimized. Figure 3A demonstrates the SST difference from CTL to EXP1, showing equatorial warming over the Pacific, with cooling in other regions, and a stronger cooling to the west of Mexico, which resembles an "El Niño-like pattern. Experiments 2-4 (EXP2-4) are designed to elucidate each component of the SST pattern in EXP1, while keeping the global mean SST the same as in EXP1. These designs allow us to examine the response of global TC frequency to SST patterns, specifically the role of equatorial cold tongue warming and cooling. EXP2-4 are as follows:

- EXP2 is "Only-cold-tongue-warming", in which cold-tongue warming is the same as in EXP1, but uniform cooling is applied elsewhere on the globe. The SST anomalies relative to CTL are shown in Fig. 3B. This experiment specifically focuses on warming over the equatorial cold tongue.
- EXP3 is "No-cold-tongue warming", designed to further examine the effect on TCs without equatorial cold-tongue warming, the opposite situation to EXP2. We remove the equatorial cold tongue and add its warming uniformly to other regions of the globe. The SST anomalies relative to CTL are shown in Fig. 3C. Except for the cold tongue warming, the remaining tropical ocean SST anomalies are qualitatively similar to those in EXP1.
- The last experiment (EXP4) is the reversed SST anomaly pattern compared to EXP1 (a "La Niña-like" pattern), where cooling occurs over the equatorial cold tongue, and warming occurs elsewhere (Fig. 3D). Note that there is also a slight enhanced warming off of the Mexican coast, opposite to the enhanced cooling in EXP1. The

SST anomalies are obtained with the reverse sign of those in EXP1 and, additionally, scale the magnitudes of the positive and negative anomalies to keep the global mean cooling the same as in EXP1 (Fig. 3D). This is why the magnitude of the anomalies is smaller in EXP4 than in EXP1. This experiment provides the opposite situation to EXP1 to further investigate the effect of equatorial cooling.

Tropical cyclone tracking

The TC tracking criteria in ACE2 identify closed contours of sea level pressure, and the center of TCs when a sea level pressure minimum occurs, and 10-meter maximum wind is above 10 m/s. The sea level pressure needs to decrease by 2 hPa within 5.5 deg. We use the TempestExtremes package to track TCs (39), with detailed criteria same as (22). TempestExtremes has two steps: the first step is to detect the center of TCs, and the second step is to connect TC locations of the same storm together in time. In HiRAM, we use a slightly different tracking criterion to be consistent with their previous study. We track TCs in HiRAM following the algorithm developed by (36), with lifetime and threshold criteria similar to (37). Because HiRAM tends to produce more TCs than observed, we only detect hurricane-level TCs in HiRAM to represent its TC activities. The criteria we use for TC detection in HiRAM are at least 72 hours of total lifetime, 48 cumulative hours of warm core, and 36 continuous hours of both warm core and max wind speed > 15.75 m/s. Hurricane-level TCs are identified if the peak intensity is over 30 m/s.

Even if we use slightly different tracking criteria in ACE2 and HiRAM, it is appropriate because we only compare the percent change of TCs in ACE2 and HiRAM relative to the model's own baseline (i.e., the model's TC number climatology), instead of comparing the absolute number of TCs. The different tracking criteria are tuned to suit each simulation model.

TCs are abundant in each major active TC basin in 1401 to 1420 (Fig. S2A), where off-equatorial sea surface temperature is relatively high (Fig. S2B). We separate TCs into 6 basins, including the Northern Indian Ocean (NIO, 45-105E, 0-30N), Southern Indian Ocean (SIO, 35-135E, 0-30S), Northwestern Pacific (NWPAC, 105-180E, 0-30N), South Pacific (SPAC, 135-270E, 0-30S), Northeastern Pacific (NEP, 180-265E, 0-30N), and North Atlantic (NATL, 265-359E, 0-30N). The domain of each basin is shown in Fig. 1B, following (22).

Seed tracking

We also track the precursor disturbance (i.e., seeds) prior to tropical cyclogenesis in ACE2 using TempestExtremes (39). Because there is no universal definition of seeds, we combine the approaches from (27, 40), based on the variables available in ACE2. The tracking criteria are based on a vorticity maximum at 850 hPa, a 99th percentile precipitation threshold, and a decrease of 1 hPa in sea level pressure within 5.5 deg. Note that the sea level pressure criterion is half of the TC definition, aiming to find the disturbances before TC genesis. We have also tried different criteria for seeds by adjusting the sea level pressure criteria to 0.5 hPa and 0.2 hPa. The key results of this paper remain qualitatively similar regardless of this threshold, as shown in Fig. S7, in that the global decrease in TC frequency is mostly dominated by the decrease in transition probability.

Analysis of the TC decadal trend

Because the year-to-year variation of TC numbers is large, we process the data to better depict the decadal trend of TCs using a 40-year low-pass Butterworth filter. The 40-year

Butterworth filter is also applied to the time series between 1351 and 1550 AD, where the beginning and ending 20 years are discarded due to the biased response function (41).

Statistical analysis

After tracking TCs in idealized SST experiments in ACE2, we perform the binomial test to quantify how significant each TC season is above or below the average TC number in the control run. Figure 3E shows, across the 40 years of each experiment, how many TC seasons are more active (magenta) or less active (green) than the CTL. If SST patterns do not affect the global TC count, there will be equal numbers of active and inactive seasons (20 years each). The p-value is obtained by how significant the result of each experiment is compared to a random distribution, shown in Fig. 3E.

The seed-probability framework

Lastly, we apply the seed-probability framework to examine what environmental condition leads to the TC frequency change. The overall probability difference between the control run and Experiment 1 in HiRAM is consistent with ACE2 (Fig. S8).

This seed-probability framework was first introduced in (26) based on aquaplanet simulations of the current climate with various warming and cooling experiments. We choose this framework to analyze the TC frequency change in paleoclimate because this framework has been applied successfully to explain TC frequency on various timescales and climates, including the seasonal cycle of TCs in the current climate (27), changes of TC frequency under global warming, and ENSO-like perturbations (28). We have also tried an alternative framework, which is the tropical cyclone genesis index (42), the same as the one used in our earlier study of ACE2 in the current climate (22), and found that the change in environmental conditions from 1401-1420 to 1461-1480 shows consistent results (not shown). Under the seed-probability framework, the number of TCs is approximated as the number of seeds multiplied by probability (Eq. 1), where the probability is calculated by

$$\text{Probability} = , \quad [2]$$

and the ventilation index (VI, 43) is quantified by the following equation:

$$\text{VI} = , \quad [3]$$

where PI represents the potential intensity, shear represents vertical wind shear, and X represents moist entropy deficit. The saturation moisture deficit used to calculate probability in Eq. [1-3] is:

$$=, \quad [4]$$

where is the saturation moist entropy at 600 hPa, and is the environmental entropy at 600 hPa, is the saturation moist entropy at the sea surface, and is the entropy of the boundary layer. Moist entropy can be calculated using the following equation:

$$, \quad [5]$$

where is the heat capacity of dry air, is the partial pressure of dry air, is the relative humidity, is the gas constant for dry air, is the gas constant for water vapor, and is the latent heat for vaporization. The potential intensity can be calculated by

, [6]

where represents surface temperature, and represents outflow temperature. The terms and represent the sea surface saturation enthalpy and the boundary layer enthalpy. Because ACE2 provides coarse vertical resolution (8 vertical levels), to accommodate this limitation when calculating potential intensity, we prescribe the outflow pressure level from the 37 vertical-level dynamical simulation HiRAM, rather than calculating it from ACE2. We obtain the outflow temperature in ACE2 based on the environmental temperature at 100 hPa for the deep convection region (SST> 70%), 400 hPa for the weak subsidence region, and 600 hPa for the strong subsidence region (SST< 10%). The choice of vertical levels for each horizontal grid is obtained by calculating the time average outflow levels from the vertically-fined HiRAM simulation with the same time period (1351-1550 AD). This approach is under the assumption that outflow levels are mostly determined by the SST, which is identical in HiRAM and ACE2.

Seed propensity index

Under the seed-probability framework, we use two approaches to quantify seeds, one of which is to explicitly track seeds, and the other is to approximate the seed density based on environmental conditions. The latter one is called the seed propensity index (SPI), developed by (26). Since vertical velocity is not the direct output of ACE2, we adopt the index by replacing vertical velocity at 500 hPa with precipitation, given that the monthly means of the two fields are often tightly correlated. Our calculation of the seed propensity index is as follows:

SPI = precip * , [7]

where precip represents precipitation rate, and Z represents normalized vorticity, which can be calculated as follows:

Z = , [8]

where f is planetary vorticity (2* sin()), is relative vorticity (, and U=20 and =0.69 are parameters fitted from aquaplanet simulations. We relate the tracked seed density to the SPI in Fig. 6.

References

1. Sobel, A. H., Wing, A. A., Camargo, S. J., Patricola, C. M., Vecchi, G. A., Lee, C. Y., & Tippett, M. K. (2021). Tropical cyclone frequency. *Earth's Future*, *9*(12), e2021EF002275.
2. Knutson, T., Camargo, S. J., Chan, J. C., Emanuel, K., Ho, C. H., Kossin, J., ... & Wu, L. (2020). Tropical cyclones and climate change assessment. *Bulletin of the American Meteorological Society*, *101*(3), E303-E322.
3. Roberts, M. J., Camp, J., Seddon, J., Vidale, P. L., Hodges, K., Vannière, B., ... & Wu, L. (2020). Projected future changes in tropical cyclones using the CMIP6 HighResMIP multimodel ensemble. *Geophysical Research Letters*, *47*(14), e2020GL088662.
4. Emanuel, K. A. (2013). Downscaling CMIP5 climate models shows increased tropical cyclone activity over the 21st century. *Proceedings of the National Academy of Sciences*, *110*(30), 12219-12224.
5. Yoshida, K., Sugi, M., Mizuta, R., Murakami, H., & Ishii, M. (2017). Future changes in tropical cyclone activity in high-resolution large-ensemble simulations. *Geophysical Research*

Letters, *44*(19), 9910-9917.
6. Yamada, Y., Kodama, C., Satoh, M., Sugi, M., Roberts, M. J., Mizuta, R., ... & Vidale, P. L. (2021). Evaluation of the contribution of tropical cyclone seeds to changes in tropical cyclone frequency due to global warming in high-resolution multi-model ensemble simulations. *Progress in Earth and Planetary Science*, *8*(1), 11.
7. Sobel, A. H., Lee, C. Y., Bowen, S. G., Camargo, S. J., Cane, M. A., Clement, A., ... & Tippett, M. K. (2023). Near-term tropical cyclone risk and coupled Earth system model biases. *Proceedings of the National Academy of Sciences*, *120*(33), e2209631120.
8. Vecchi, G. A., & Soden, B. J. (2007). Effect of remote sea surface temperature change on tropical cyclone potential intensity. *Nature*, *450*(7172), 1066-1070.
9. Eusebi, R., Vecchi, G. A., Yang, W., & Fueglistaler, S. (2025). The Influence of Patterned Warming and CO 2 on North Atlantic Hurricane Frequency. *Journal of Climate*, *38*(19), 5391-5410.
10. Levin, E. L., Vecchi, G., & Yang, W. (2025). Influence of sea surface temperature patterns and mean warming on past and future Atlantic hurricane activity.
11. Lin, J., Lee, C. Y., Camargo, S. J., Sobel, A. H., & Zhuo, J. Y. (2025). The response of tropical cyclone hazard to natural and forced patterns of warming. *npj Climate and Atmospheric Science*, *8*(1), 109.
12. Zhang, G., Lin, K. E., Fu, D., Knutson, T., Franke, J., & Tseng, W. L. (2025). Chinese Historical Documents Reveal Multi-Century Seasonal Shifts in Tropical Cyclone Landfalls. *arXiv preprint arXiv:2502.00276*.
13. Lin, K. H. E., Tseng, W. L., Lin, Y. S., Lee, C. Y., Lin, Y. H., Hsu, H. H., & Wang, P. K. (2025). Intensified tropical cyclone activity in East Asia during the Maunder (solar) Minimum. *Proceedings of the National Academy of Sciences*, *122*(52), e2419759122.
14. Schmitt, D., Gischler, E., Melles, M., Wennrich, V., Behling, H., Shumilovskikh, L., ... & Birgel, D. (2025). An annually resolved 5700-year storm archive reveals drivers of Caribbean cyclone frequency. *Science Advances*, *11*(11), eads5624.
15. Yang, W., Wallace, E., Vecchi, G. A., Donnelly, J. P., Emile-Geay, J., Hakim, G. J., ... & Winkler, T. S. (2024). Last millennium hurricane activity linked to endogenous climate variability. *Nature communications*, *15*(1), 816.
16. Tardif, R., Hakim, G. J., Perkins, W. A., Horlick, K. A., Erb, M. P., Emile-Geay, J., ... & Noone, D. (2019). Last Millennium Reanalysis with an expanded proxy database and seasonal proxy modeling. *Climate of the Past*, *15*(4), 1251-1273.
17. Cresswell-Clay, N., Liu, B., Durran, D. R., Liu, Z., Espinosa, Z. I., Moreno, R. A., & Karlbauer, M. (2025). A deep learning earth system model for efficient simulation of the observed climate. *AGU Advances*, *6*(4), e2025AV001706.
18. Kochkov, D., Yuval, J., Langmore, I., Norgaard, P., Smith, J., Mooers, G., ... & Hoyer, S. (2024). Neural general circulation models for weather and climate. *Nature*, *632*(8027), 1060-1066.
19. Watt-Meyer, O., Henn, B., McGibbon, J., Clark, S. K., Kwa, A., Perkins, W. A., ... & Bretherton, C. S. (2025). ACE2: accurately learning subseasonal to decadal atmospheric variability and forced responses. *npj Climate and Atmospheric Science*, *8*(1), 205.
20. Clark, S. K., Watt-Meyer, O., Kwa, A., McGibbon, J., Henn, B., Perkins, W. A., ... & Bretherton, C. S. (2025). ACE2-SOM: Coupling an ML atmospheric emulator to a slab ocean and learning the sensitivity of climate to changed CO2. *Journal of Geophysical Research: Machine Learning and Computation*, 2(4), e2024JH000575.
21. *Brenowitz, N. D., Ge, T., Subramaniam, A., Manshausen, P., Gupta, A., Hall, D. M., ... & Pritchard, M. S. (2025). Climate in a bottle: Towards a generative foundation model for the kilometer-scale global atmosphere. arXiv preprint arXiv:2505.06474.*
22. Chien, M. T., Barnes, E. A., & Maloney, E. D. (2025). Modulation of tropical cyclogenesis on subseasonal-to-interannual timescales in the deep-learning climate emulator ACE2. *Machine*

Learning: Earth, *1*(1), 015008.
23. Chien, M. T., Barnes, E. A., & Maloney, E. D. (2025). Modulation of Tropical Cyclogenesis by the Convectively Coupled Kelvin Waves: Insights from Data-driven Climate Emulator ACE2. *Geophysical Research Letters*, *53*(2), e2025GL117387.
24. Duan, S., Zhang, J., Bonfils, C., & Pallotta, G. (2025). Testing NeuralGCM's capability to simulate future heatwaves based on the 2021 Pacific Northwest heatwave event. *npj Climate and Atmospheric Science*, 8(1), 251.
25. Meng, Z., Hakim, G. J., Yang, W., & Vecchi, G. A. (2025). Deep learning atmospheric models reliably simulate out-of-sample land heat and cold wave frequencies. *arXiv preprint arXiv:2507.03176*.
26. Hsieh, T. L., Vecchi, G. A., Yang, W., Held, I. M., & Garner, S. T. (2020). Large-scale control on the frequency of tropical cyclones and seeds: A consistent relationship across a hierarchy of global atmospheric models. *Climate Dynamics*, *55*(11), 3177-3196.
27. Yang, W., Hsieh, T. L., & Vecchi, G. A. (2021). Hurricane annual cycle controlled by both seeds and genesis probability. *Proceedings of the National Academy of Sciences*, *118*(41), e2108397118.
28. Hsieh, T. L., Yang, W., Vecchi, G. A., & Zhao, M. (2022). Model spread in the tropical cyclone frequency and seed propensity index across global warming and ENSO-like perturbations. *Geophysical Research Letters*, *49*(7), e2021GL097157.
29. Brennan, M. K., & Hakim, G. J. (2022). Reconstructing Arctic sea ice over the Common Era using data assimilation. *Journal of Climate*, *35*(4), 1231-1247.
30. Toohey, M., & Sigl, M. (2017). Volcanic stratospheric sulfur injections and aerosol optical depth from 500 BCE to 1900 CE. *Earth System Science Data*, *9*(2), 809-831.
31. *Gray, W.M., 1975. Tropical cyclone genesis.*
32. Van Loon, S., Rugenstein, M., & Barnes, E. A. (2025). Reanalysis-based global radiative response to sea surface temperature patterns: Evaluating the Ai2 climate emulator. *Geophysical Research Letters*, *52*(14), e2025GL115432.
33. Hsieh, T. L., Vecchi, G. A., Wang, C., Yang, W., Zhang, B., & Soden, B. J. (2024). Dependence of tropical cyclone seeds and climate sensitivity on tropical cloud response. *Science advances*, *10*(37), eadi2779.
34. Hersbach, H., Bell, B., Berrisford, P., Hirahara, S., Horányi, A., Muñoz-Sabater, J., ... & Thépaut, J. N. (2020). The ERA5 global reanalysis. *Quarterly journal of the royal meteorological society*, *146*(730), 1999-2049.
35. Bonev, B., Kurth, T., Hundt, C., Pathak, J., Baust, M., Kashinath, K., & Anandkumar, A. (2023, July). Spherical fourier neural operators: Learning stable dynamics on the sphere. In *International conference on machine learning* (pp. 2806-2823). PMLR.
36. Harris, L. M., Lin, S. J., & Tu, C. (2016). High-resolution climate simulations using GFDL HiRAM with a stretched global grid. *Journal of Climate*, *29*(11), 4293-4314.
37. Zhao, M., Held, I. M., Lin, S. J., & Vecchi, G. A. (2009). Simulations of global hurricane climatology, interannual variability, and response to global warming using a 50-km resolution GCM. *Journal of Climate*, *22*(24), 6653-6678.
38. Sullivan, R. M., Wallace, E., Dee, S., Vecchi, G. A., Yang, W., & Emanuel, K. (2025). Multi-centennial spatial coherency among Atlantic tropical cyclones from simulated and reconstructed storm records. *Geophysical Research Letters*, 52, e2025GL116642
39. Ullrich, P. A., & Zarzycki, C. M. (2017). TempestExtremes: A framework for scale-insensitive pointwise feature tracking on unstructured grids. *Geoscientific Model Development*, *10*(3), 1069-1090.
40. Moon, J., Kim, D., Wing, A. A., Camargo, S. J., Emlaw, G. N., Starr, J. C., & Cha, D. H. (2025). Tropical cyclone seed disturbances in ERA5. *Journal of Climate*, *38*(18), 4625-4639.
41. Butterworth, S. (1930). On the theory of filter amplifiers. *Wireless Engineer*, 7(6), 536-541.
42. Tippett, M. K., Camargo, S. J., & Sobel, A. H. (2011). A Poisson regression index for tropical

cyclone genesis and the role of large-scale vorticity in genesis. *Journal of Climate*, *24*(9), 2335-2357.
43. Tang, B., & Emanuel, K. (2012). A ventilation index for tropical cyclones. *Bulletin of the American Meteorological Society*, 93(12), 1901-1912.

Acknowledgments

We acknowledge scientific discussions with Emma Levin, Prof. Greg Hakim, Dr. Jihong Moon, and Prof. Daehyun Kim that benefit this work.

Funding:

Heising-Simons Foundation grant #2023-4720
National Oceanic and Atmospheric Association (NOAA) CVP grant NA22OAR4310609
National Science Foundation (NSF) grant AGS-2217785

Author contributions:

Conceptualization: MC, EAB, EDM
Methodology: MC, WY
Investigation: MC, WY
Visualization: MC
Writing—original draft: MC
Writing—review & editing: EAB, EDM, WY, &GAV

Competing interests: All other authors declare they have no competing interests.

Data and materials availability: All analysis code is available on GitHub at https://github.com/muting-chien/Paleo_global_TC_1351_1550_public.

Figures and Tables

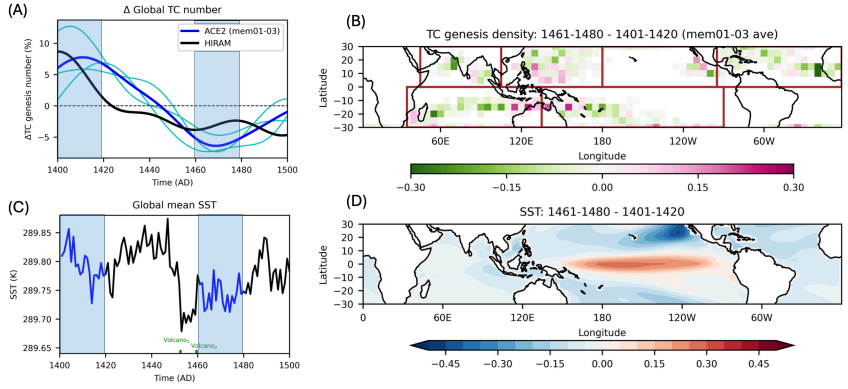

Figure 1. Changes in global TCs and SSTs in the 15th century. (A) Time series of the

percentage change of global tropical cyclone numbers from 1401 to 1500. The light blue lines represent each ACE2-ERA5 ensemble member, with the dark blue line representing the ensemble mean. The black line represents the hurricane-level tropical cyclones in HiRAM. (B) The change in genesis density of tropical cyclones from 1401-1420 to 1461-1480 averaged across three ensemble members. The red box marks each basin. The top row from left to right represents the North Indian Ocean (NIO), the North Western Pacific (NWPAC), the North Eastern Pacific (NEPAC), and the North Atlantic (NATL), while the bottom row represents the South Indian Ocean (SIO) and the South Pacific (SPAC). (C) The global mean sea surface temperature time series from 1401 to 1500. The green horizontal lines at the bottom indicate the two volcanic eruptions in 1452-1453 and 1459-1460. (D) The change in mean sea surface temperature from 1401-1420 to 1461-1480. The light blue shadings in (A) and (C) represent the High and Low periods we focus on in this study, depicting higher and lower TC numbers in the 15th century.

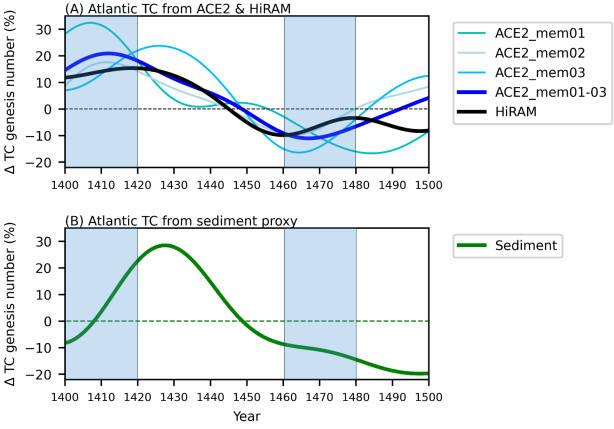

Fig. 2. Time series of Atlantic tropical cyclone (TC) number change in the 15th century. (A) The light blue lines represent each ACE2-ERA5 ensemble member, with the dark blue line representing the ensemble mean. The black line represents the hurricane-level tropical cyclones in HiRAM. The light-blue shading represents the High and Low periods. (B) The green line represents the sediment proxy TC anomalies. TC anomalies from each data are applied with a 40-year low-pass filter.

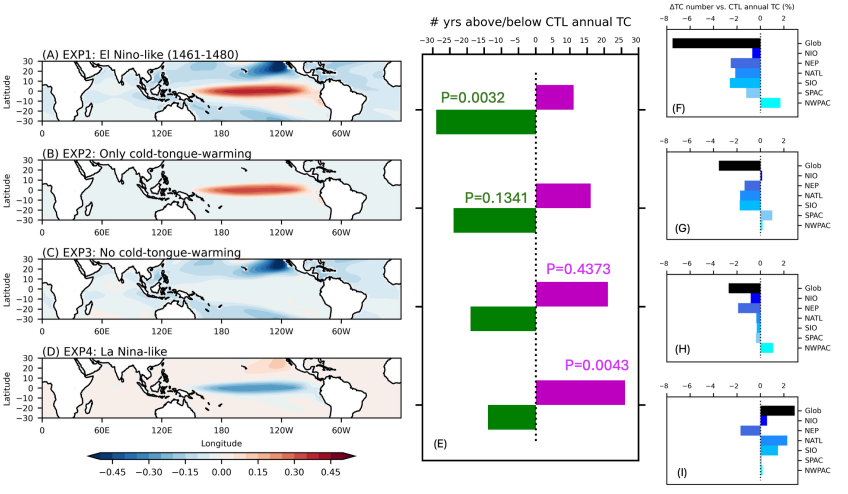

Fig. 3. Idealized sea surface temperature (SST) experiments and tropical cyclone response. (A-D) The mean SST difference compared to the control simulation (CTL) (1401-1420): (A) Experiment 1: averaged SST between 1461-1480 (El Niño-like), (B) Experiment 2: only cold-tongue-warming, (C) Experiment 3: no cold-tongue-warming, and (D) Experiment 4: La Niña-like. (E) The number of years that the tropical cyclone (TC) counts in each experiment are above (magenta bar) or below (green bar) the mean value of the TC counts in CTL. P-value for the binomial test is displayed. (F-I) The percentage change in the mean of TC number from CTL to each experiment globally (black bar) and in each basin (different blue bars). The percentage change in each basin is relative to the mean global TC number in CTL.

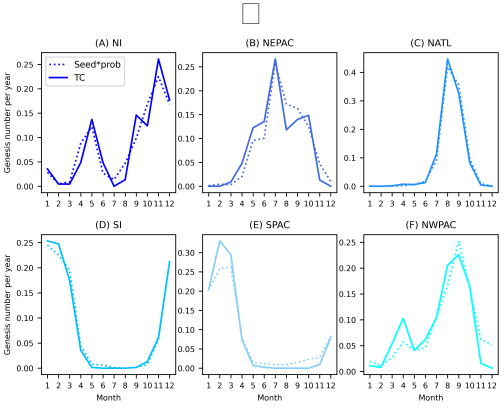

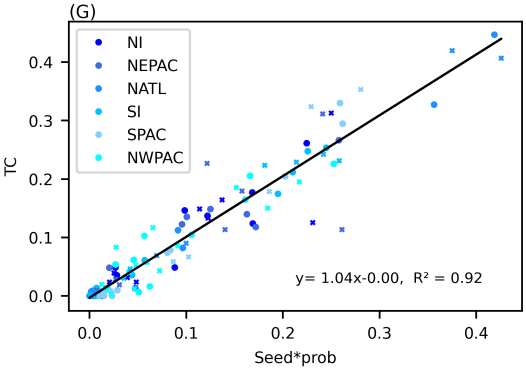

Fig. 4. Annual cycle of actual TC number and estimated TC number (i.e., seed multiplied by transition probability) after normalization. (A-F) Annual cycle of actual TC number (solid line) and estimated TC number (dotted line) in the control run in each basin: (A) North Indian Ocean (NI), (B) North Eastern Pacific (NEPAC), (C) North Atlantic (NATL), (D) Southern Indian Ocean (SIO), (E) Southern Pacific Ocean (SPAC), and (F) North Western Pacific (NWPAC). (G) Scatter plot between the annual cycle of the actual (y-axis) and estimated (x-axis) TC number for each basin. Dots represent the control run, while crosses represent Experiment 1. The linear regression line is displayed.

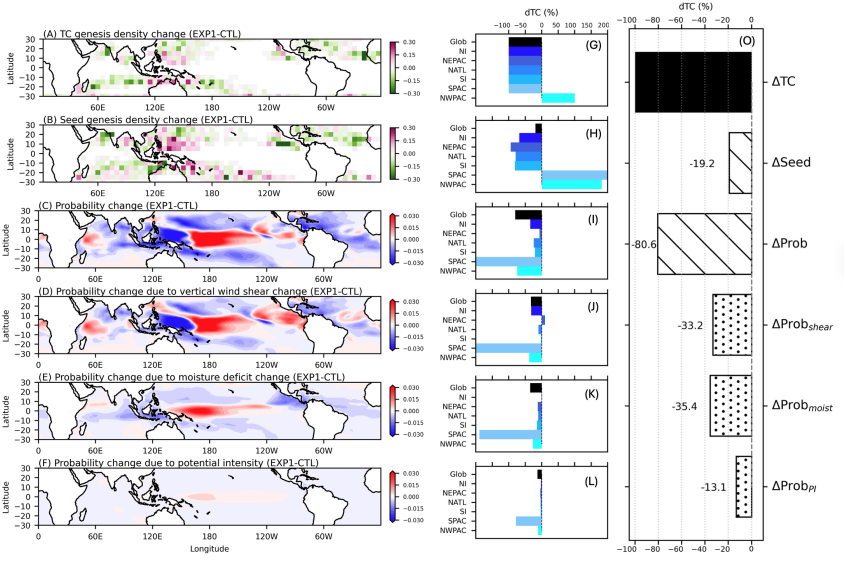

Fig. 5. Difference in seed and probability from CTL to EXP1. (A) The genesis density of tropical cyclones, (B) the genesis density of seeds, (C) the calculated transition

probability from seed to tropical cyclones based on potential intensity, saturation moisture deficit, and vertical wind shear, (D-F) the calculated transition probability with a single variable in Experiment 1, while the other environmental factors are kept the same as in CTL. The single varying factor is: (D) potential intensity, (E) saturation moisture deficit, (F) vertical wind shear. (G-L) The percentage change of TC genesis number from CTL to Experiment 1 in each basin due to each factor: (G) actual TC number change, (H) seed density change, (I) probability change, (J) potential intensity change that changes probability, (K) saturation moisture deficit change that changes probability, (L) vertical wind shear change that changes probability. (O) The percentage change of the global TC number (solid bar) due to changes in seeds and probability (slanted hatch). The change in probability can be separated by changes in shear, moisture, and potential intensity (dotted hatch).

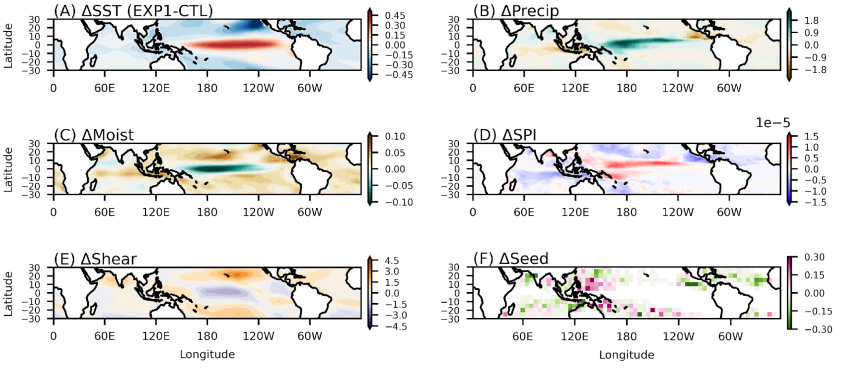

Fig. 6. Difference in environmental conditions and seeds from CTL to EXP1. (A) Sea surface temperature, (B) precipitation, (C) saturation moisture deficit, (D) seed propensity index based on vorticity and precipitation, (E) vertical windshear, and (F) seed genesis density.

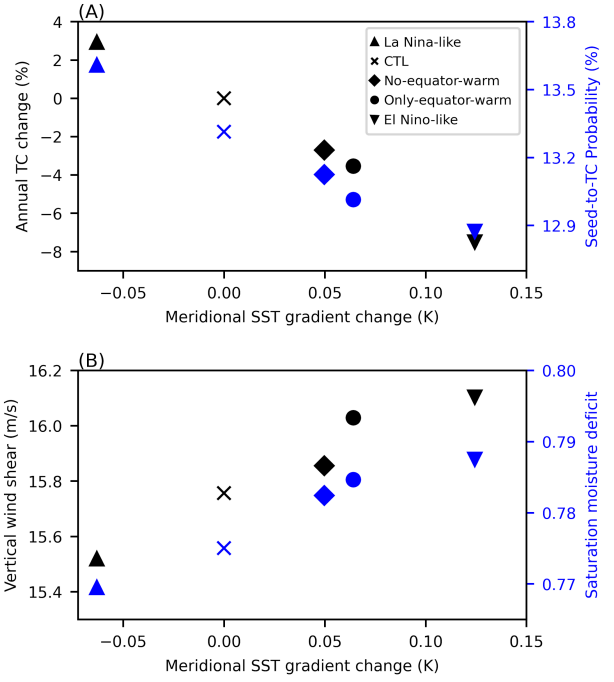

Fig. 7. Summary of the global TC and environmental conditions from each SST experiment. The X-axis represents the meridional SST gradient change from the control run, calculated from the change in SST of the equatorial region (10S-10N) minus the change in SST in the off-equatorial region (10-30N/S) compared to the control run. (A) The Y-axis on the left (black) represents the annual TC number change from the control simulation, and the Y-axis on the right (blue) represents the Seed-to-TC probability. (B) The Y-axis on the left (black) represents the vertical wind shear, and the Y-axis on the right (blue) represents the saturation moisture deficit. The global mean of each quantity on the Y-axis excludes 5S-5N and the Southeastern Pacific and South Atlantic regions, where TC activity is rare.

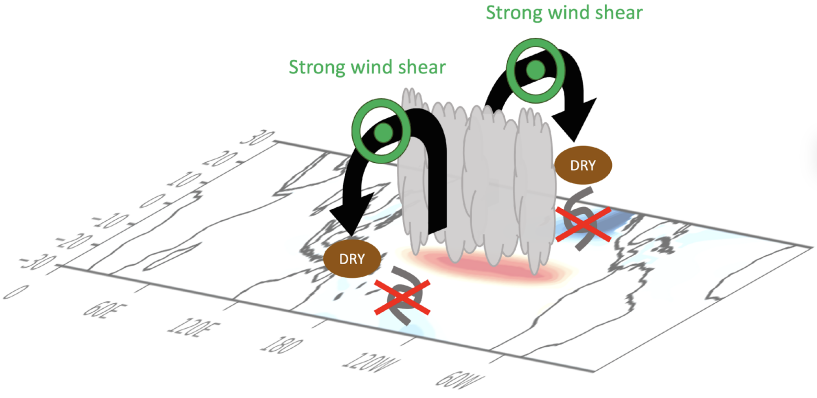

Fig. 8. Schematic of the decrease in global TC frequency under an El Niño-like SST trend. Equatorial warming induces stronger meridional circulation, stronger wind shear, and a drier midtroposphere, which are detrimental to TC genesis.